Annealing treatment of a Gd-containing stainless steel and the corrosion behavior

Manman Xie[1,2†], Dongxiao Jia[3,4†], Xilin Jia[2,4], Fei Zhao[1], Tian Liang[3,5*], Yangtao Zhou[2*]

[1] School of Materials Science and Engineering, Taiyuan University of Science and Technology, Taiyuan 030024, China; [2] Shenyang National Laboratory for Materials Science, Institute of Metal Research, Chinese Academy of Sciences, Shenyang 110016, China; [3] Shi-Changxu Innovation Center for Advanced Materials, Institute of Metal Research, Chinese Academy of Sciences, Shenyang 110016, China; [4] School of Materials Science and Engineering, University of Science and Technology of China, Shenyang 110016, China; [5] CAS Key Laboratory of Nuclear Materials and Safety Assessment, Institute of Metal Research, Chinese Academy of Sciences, Shenyang 110016, China

† These authors contributed equally to this work
* Corresponding authors: Tian Liang, tliang@imr.ac.cn; Yangtao Zhou, ytzhou@imr.ac.cn

Abstract: In this paper, the microstructures and corrosion behaviors of a 1.0 wt.% Gd duplex stainless steel annealed at different temperatures were studied. Electron microscopy revealed that the content of secondary Gd-containing phase was increased along with the increasing annealing temperatures and then decreased at 1080°C as an inflection point. An M-Gd (M=Fe, Cr, Ni) intermetallic with M_3Gd as the core phase and $M_{12}Gd$ as the shell was the main type of secondary phase in the sample annealed at 1080°C. In the sample annealed at 1140°C, M_3Gd phase was dominant. The corrosion behaviors of the two annealed steel samples were analyzed in NaCl, HCl and H_3BO_3 solutions. It showed that the sample annealed at 1140°C had lower corrosion rate. M_3Gd was more electrochemically active than $M_{12}Gd$ when the sample was immersed in NaCl and HCl solutions, but more noble in H_3BO_3 solution.

Key words: Neutron-absorbing duplex stainless steel; Annealing treatment; Gd-containing intermetallics; Corrosion

Development of nuclear industry inevitably generates a large amount of highly radioactive spent nuclear fuel (SNF) waste. During the transport and storage process of SNF, neutron-absorbing structural materials have been widely used for the containers, racks and transport parts[1-3]. Fe-based[4-7], Ni-based[8-11] alloys and Al-matrix composites[12-16] containing neutron-absorbing elements are the most used materials. For wet-storage method, the SNF should be immersed in boron acid solution for years. Therefore, corrosion resistance of the neutron-absorbing materials, in addition to their strength, ductility, and processing ability should be seriously considered.

Fe and Ni-based alloys, in particular stainless steels (SS), are the most prominent candidates for the application. Among them, boron-containing stainless steels have been used widely. However, the shortage of the material is obvious: on the one hand, the limited solubility of boron in stainless steels pre-

vents the production of alloys with more than 2.25 wt% boron [17]; on the other hand, the ductility of the early borated stainless steel decreases with the increasing volume fraction of the boron-containing secondary phases[18]. Additionally, He gas bubbles will be generated in B-containing metals by long-term neutron irradiation, which is a safety risk for structural materials[19]. In recent years, gadolinium (Gd)-containing alloys received increasing attention due to higher thermal neutron absorption ability and being free of He generation. The thermal neutron absorption cross-sections of [155]Gd and [157]Gd are 16 and 66 times higher than that of [10]B, respectively20[20,21]. A series of Gd-containing Fe and Ni alloys have been used and studied in the past decades and Gd-containing steels are particularly preferred from the economic consideration[22]. Since Gd has very low solubility limit in the Fe and Ni-based matrices, it usually presents in the form of Gd-containing sec-

ondary phases, which have an significant impact on the corrosion resistance and mechanical properties of the alloys[6,11,23,24]. According to the literatures, M_3Gd, M_5Gd, $M_{17}Gd_2$, etc. are the commonly found secondary phases in Gd-containing steels[25,26].

The types of metallic M-Gd phases are closely related to the compositions and the heat-treatment process of the steel matrix[27]. Kang et al. designed three Gd-containing alloy steels and found a new type of precipitate $M_{12}Gd$ which had higher melting temperature than other precipitates and would be utilized to alloys with better hot workability and weldability[6]. Wang et al. studied the effects of different solution treatment temperatures on the secondary phase and hardness of Gd-stainless steel, and found the "gray" phase was wrapped with "bright white" phase. After 1000~1070℃ solid solution treatment, the "bright white" phase gradually transformed into "gray" phase[28].

On the other hand, the corrosion resistance of the steels is also highly influenced by the Gd-containing phases. In Gd-316 SS, $(Fe,Cr,Ni)_3Gd$ is usually seen along grain boundaries. The precipitation of $(Fe,Ni,Cr)_3Gd$ will result in a Cr-rich and Ni-poor zone in the steel, and destroy the stability of the matrix[29]. Lister et al. found that the preferential dissolution of Gd-containing intermetallics reduced the corrosion resistance of the steel matrix[8]. However, it was also reported that the addition of a small amount of Gd to mild steels and duplex stainless steels was conducive to improving the corrosion resistance of the steel[30].

In the present study, a 1.0 wt.% Gd-containing duplex stainless steel was prepared. The material was annealed at different temperatures and the secondary phases in these samples were investigated by electron microscopic techniques. In addition, the corrosion resistance related to the intermetallics was studied in various aqueous environments. This research is believed to provide fundamental knowledge for the design and fabrication of Gd-containing alloys used for SNF transport and storage.

1 Material and methods

1.1 Material

The test material was Gd-containing duplex stainless steel produced by vacuum induction melting process. The cast ingot weighted about 20kg with a diameter about 150 mm. The composition of duplex stainless steels was determined by inductively coupled plasma mass spectrometry (ICP-MS, 8900 Agilent), and the contents of carbon and oxygen was determined by Carbon/Sulfur analyzer (CS844, Leco) and Oxygen/Nitrogen & Hydrogen analyzer (ONH836, Leco), respectively. The chemical compositions of the as-cast steel are listed in Table 1.

Table 1 Chemical compositions of the Gd-containing duplex

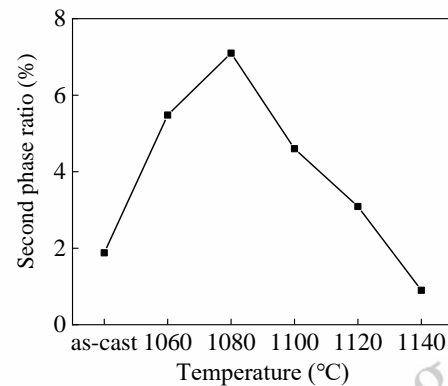| Stainless steel alloy (wt.%)									
Alloy	Cr	Ni	Mo	Mn	Si	C	O	Gd	Fe
2308	23.7	8.2	1.2	1.6	0.4	0.024	0.0034	1	Bal

Fig.1 Statistic measurement of the area fractions of Gd-containing particles in the steel annealed at different annealing temperatures

In the temperature range between 1060℃ and 1140℃, a series of heat-treatment conditions have been tested. The samples annealed at 1080℃ and 1140℃ for 30 minutes showed the most pronounced difference in the volume fraction of secondary phases and were finally chosen to investigate. The samples were named as 1080 and 1140. The specimens with a size of 10 mm×10 mm×10 mm were cut from the centre of the obtained samples.

1.2 Microstructural characterization

The specimens were mechanically ground using SiC abrasive paper from 400# to 2000#, and polished using a water-based diamond suspension containing 2.5 μm particles to obtain a mirror finish. The microstructures of the steel samples were analyzed by a scanning electron microscope (SEM, Zeiss-Supra 35). Chemical composition of the secondary phase and matrix was analyzed using energy dispersive X-ray spectroscopy (EDS) attached to the SEM. The phase distribution was characterized using an X-ray diffractometer (XRD) with Cu Kα radiation (Rigaku Ultima IV, Japan), 30 kV, 15 mA, λ = 0.15406 nm, 2θ = 40 °–100 °. The area fraction of the secondary phase was analyzed using Image J software. A Thermo Fisher Talos F200X Transmission electron microscope (TEM) was used to determine the crystallographic information of the Gd-containing phases. TEM specimen discs with a diameter of 3 mm were ground using silicon carbide papers, dimpled and finally thinned by ion-milling system Gatan PIPS 695.

1.3 Corrosion test

Potentiodynamic polarization tests were carried out with an electrochemical workstation (Gamry Reference 600+). The standard three-electrode system was used with the saturated calomel electrode as the reference electrode, the platinum electrode as the auxiliary electrode, and the packaged sample as the working electrode. The specimen ($10 \times 10 \times 1$ mm^3) for the working electrode was connected to Cu wire and cold mounted by epoxy resin. The exposed area of the working electrode was controlled to 1 cm^2. The mounted specimens were ground using SiC paper up to 2000#. The corrosion tests were repeated at least 3 times for each specimen in order to confirm the reproducibility of the experiment.

Corrosion behavior of the Gd-containing duplex stainless steels was examined through potentiodynamic polarization tests. For the polarization tests, 100 ppm NaCl solution[9,31,32], 0.36M HCl solution[33] (pH $\approx$ 0.44) and H$_3$BO$_3$ solution[12,34] at 2700-ppm boron (pH $\approx$ 4.88) were used. H$_3$BO$_3$ solution was used in order to simulate spent fuel pool environment. NaCl and HCl solutions were used to investigate the polarization behaviors of the samples in a neutral Cl$^-$-containing solution and a solution with low pH.

In addition, the corrosion resistance of the samples was also studied by immersion tests in NaCl, HCl, and H$_3$BO$_3$ solutions, respectively. The steel samples were mechanically ground using SiC abrasive paper up to 2000#, and polished using a water-based diamond suspension containing 2.5 μm particles to obtain a mirror finish. After corrosion tests, the corrosion morphologies were examined by SEM. Table 2 summarizes conditions for the corrosion tests.

Table 2 Test conditions used for the potentiodynamic polarization and immersion tests

Test conditions	
Potentiodynamic polarization tests	**Immersion tests**
100 ppm NaCl, 25±1°C	100 ppm NaCl, 40±1°C, 10h
0.36 M HCl, 25±1°C	0.36 M HCl, 40±1°C, 4h
(B=2700 ppm) H$_3$BO$_3$, 25±1°C	(B=2700 ppm) H$_3$BO$_3$, 40±1°C, 3h

2 Results and Discussion

2.1 Microstructures

The as-cast Gd-containing duplex stainless steel and the annealed samples (at 1080°C and 1140°C for 30 min) were firstly analyzed by XRD, as shown in Fig. 2. The XRD results indicate that the phase compositions in the samples annealed at different temperatures all include α-ferrite, γ-austenite and Gd-containing phases. The characteristic diffraction peaks of α-steel, i.e. $(110)_\alpha$, $(200)_\alpha$ and $(211)_\alpha$, and the peaks of γ-phase i.e. $(111)_\gamma$, $(200)_\gamma$, $(311)_\gamma$ and $(220)_\gamma$, could be clearly seen from the spectra. The weak peaks marked by 'o' were the secondary phases.
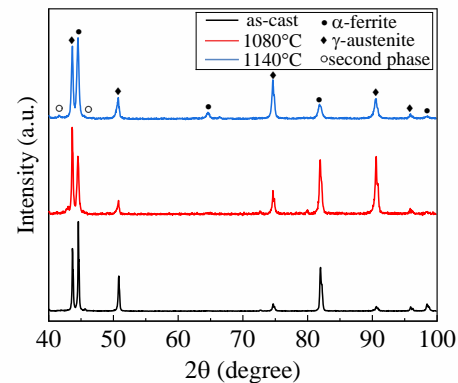

Fig.2 X-ray diffraction patterns of the as-cast steel sample (black), annealed samples 1080 (red) and 1140 (blue)

SEM-BSE images of the alloys taken at low and high magnifications are displayed in Figs. 3(a)-(c) and Figs. 3(d)-(f), respectively. The production of back-scattered electrons differs based on the weight of the element, therefore BSE image is generally used to reveal the distribution of various elements in samples. Gd has a relatively higher atomic weight than other elements in the steel. According to the contrast difference, the bright Gd-containing phase could be easily distinguished from the steel matrix. In the matrix, the two steel phases were also distinguishable, i.e. the dark grey matrix was the ferrite (α) phase and the light grey one was the austenite (γ) phase. The austenite was continuously long and elliptically distributed on the continuous ferrite (α) phase. It's worth noting that the Gd-containing secondary phases could be classified into two types as well: single-phase particles and dual phases (core-shell structure) particles. In the latter particle, the central part possessed higher contrast, indicating it was a Gd-rich compound.

According to Fig. 1, the content of Gd-containing particles in the sample 1080 was about 7.12% which was higher than that in the as-cast sample and 1140. A closer inspection (Fig. 3(d)-(f)) revealed that most of the secondary phases in the as-cast sample was Gd-rich phase and the dual-phases particles with Gd-rich core were the dominant in the sample 1080. However, when the annealing temperature was set to 1140°C, the Gd-lean particles were transformed to Gd-rich ones. The particle size was statistically decreased and the smaller ones were mainly Gd-rich phase. Only a small fraction of the particles showed a thin Gd-lean fringe. The area fraction of the two types of M-Gd phases were measured and given in Fig. 4 (a). In addition, the area fraction of the α and γ phases in the steel matrix were measured as well (Fig. 4 (b)). The area fraction of austenite in the matrix decreased from 62% to about 48% with the increase of annealing treatment temperature.
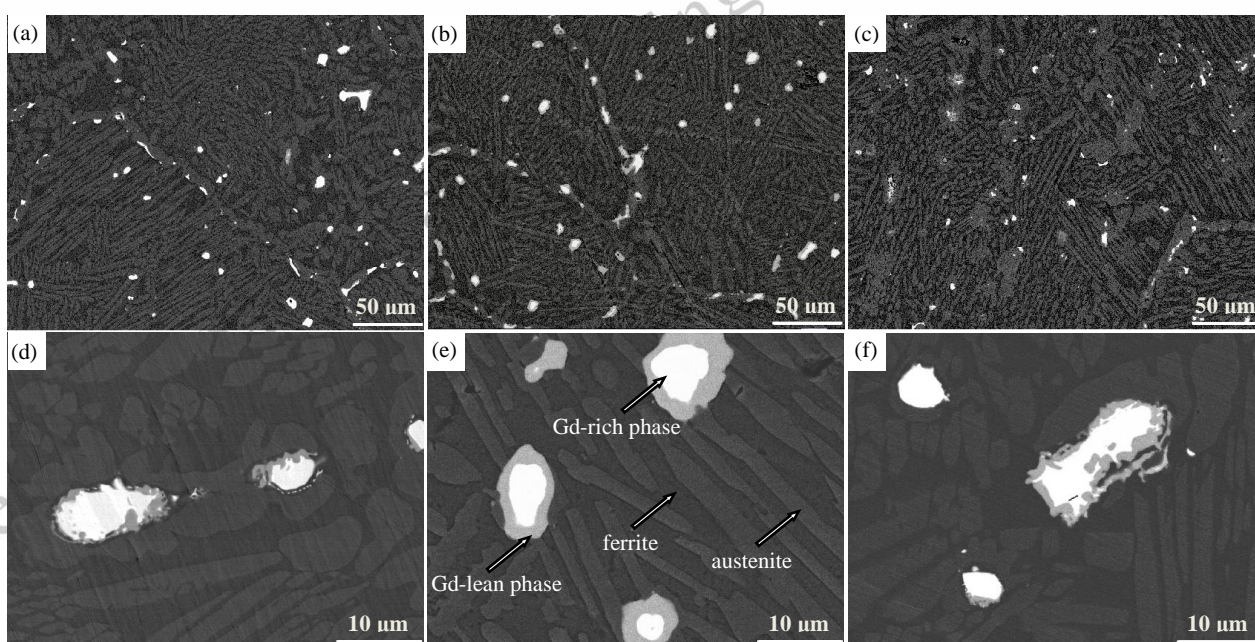
Fig. 3 Microstructures of the as-cast and annealed steel samples: (a) and (d) SEM-BSE images of the as-cast steel. The Gd-containing intermetallics are mainly Gd-rich ones and distribute in the austenitic grains and along the austenite/ferrite boundaries; (b) and (e) SEM-BSE images of the sample 1080. The core-shell structure of the M-Gd particles is obviously seen. The Gd-rich phase (white) is wrapped with Gd-lean shell (bright grey); (c) and (f) SEM-BSE images of the sample 1140. The size of secondary phase statistically decreased and the smaller ones are mainly Gd-rich phase
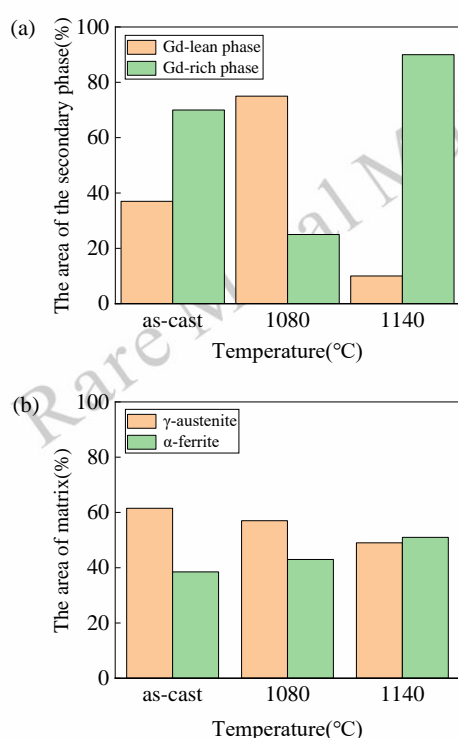

Fig. 4 Quantitative analysis on the area ratios of Gd-containing phases and matrix in the three steel sample: (a) Gd- containing phases; (b) Austenite and ferrite

To determine the chemical compositions of the Gd-containing compounds, EDS analysis was performed on each sample. The constituent elements and atomic ratio of the two secondary phases and matrix were given in Table 3. The values shown in Table 3 were the average ones based on statistical measurements on 3 individual samples. Gd was not detected in the matrix which was mainly enriched in Fe, Cr and Ni elements. The two secondary phases with different contrast were mainly composed of Fe, Cr, Ni, Gd, Mn and Si elements. The Gd-rich phase was rich of Ni and the Gd-lean phase was rich in Fe and Cr. According to the (Fe+Ni+Cr)/Gd atomic ratio, the white Gd-rich phase was estimated to be M_3Gd, where M denotes transition metallic elements, while the grey white compound was $M_{12}Gd$ or $M_{11}Gd$.

To determine the crystallographic structures of the two Gd-containing intermetallics, the steel samples were then characterized by TEM. Figs. 5(a-c) show the TEM micrograph and selected-area electron diffraction (SAED) pattern of Gd-containing compounds. A tetragonal structure with lattice parameters a=0.86 nm, c=0.48 nm could be determined according to the diffraction pattern in Fig. 5(b). Judged by the lattice parameters and the chemical compositions, the Gd-lean phase could be determined as $M_{12}Gd$ phase[6]. The diffraction pattern acquired from the Gd-rich phase is shown in Figs. 5(c). The crystalline structure of the compound was in line with M_3Gd which is a hexagonal phase[6,35]. EDS mapping under the TEM platform was also carried out to investigate the composition distributions in the two Gd-phases. As shown in Fig. 6, the phase boundary area was chosen to be analyzed. The EDS results con-

firmed the enrichment of Fe and Cr in the M_{12}Gd phase and the Ni-enrichment in M_3Gd.

2.2 Corrosion behaviors

Since the compositional and structural inhomogeneity in the as-cast steel often induced the uncertainty of corrosion data, only the annealed steel samples were tested and compared in this section. Potentiodynamic polarization curves of the annealed stainless steel measured in a 100 ppm NaCl solution are shown in Fig. 7(a). The current peaks, such as the ones appeared at 0.06 and 0.27 V_{SCE}, were attributed to dissolution of the secondary Gd-containing phases[8,36]. The two specimens in the dilute NaCl solutions did not exhibit active-passive transition.

Table 3 Chemical compositions (wt.% and at.%) of the alloy matrix and the Gd-containing secondary phases

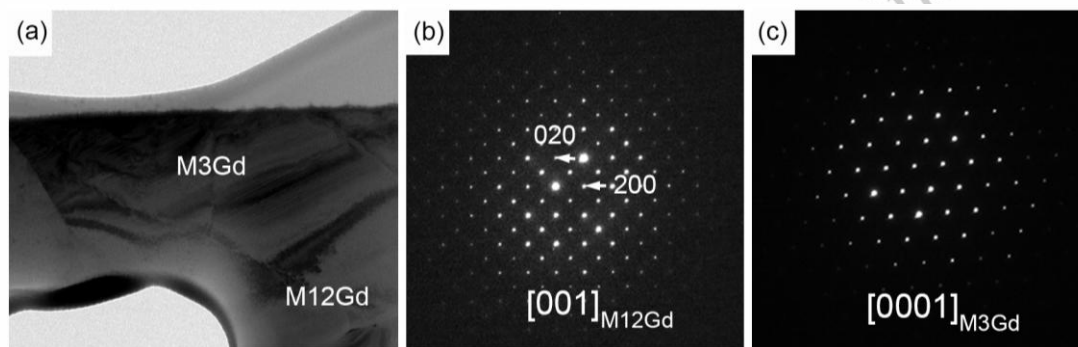| Position	Chemical compositions								[Fe+Ni+Cr]/Gd at.% ratio
	wt.%				at.%				
	Fe	Ni	Cr	Gd	Fe	Ni	Cr	Gd	
Core	17.84	36.98	3.04	46.56	18.48	32.53	3.98	18.13	3.03
Shell	44.90	16.33	14.03	19.53	44.91	11.59	16.69	6.31	11.59
ferrite	62.46	7.99	22.78	-	53.22	6.47	20.85	-	-
austenite	61.09	5.73	25.85	-	51.07	4.56	23.21	-	-

Fig. 5 TEM characterization on the Gd-containing intermetallics: (a) bright-field micrograph of a dual-phase compound; (b) SAED pattern of the M_{12}Gd phase; (c) SAED pattern of a M_3Gd phase
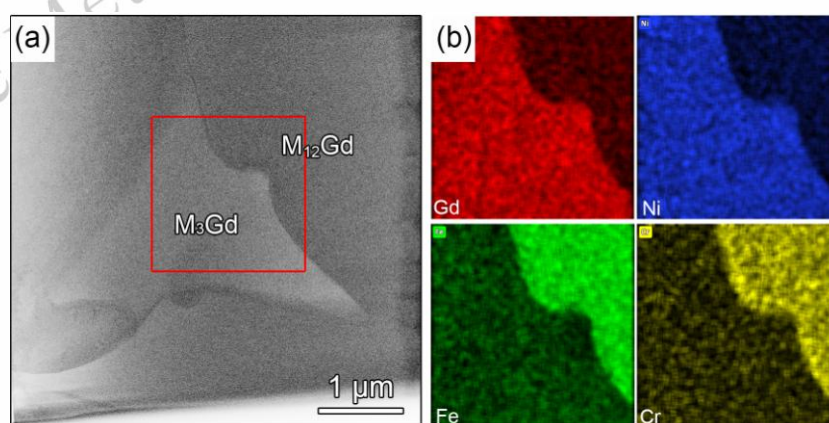

Fig. 6 HAADF-STEM image and the corresponding EDS maps of a dual-phase intermetallic: (a) HAADF STEM image; (b) The distributions of elements Gd, Ni, Fe and Cr characterized by EDS mapping
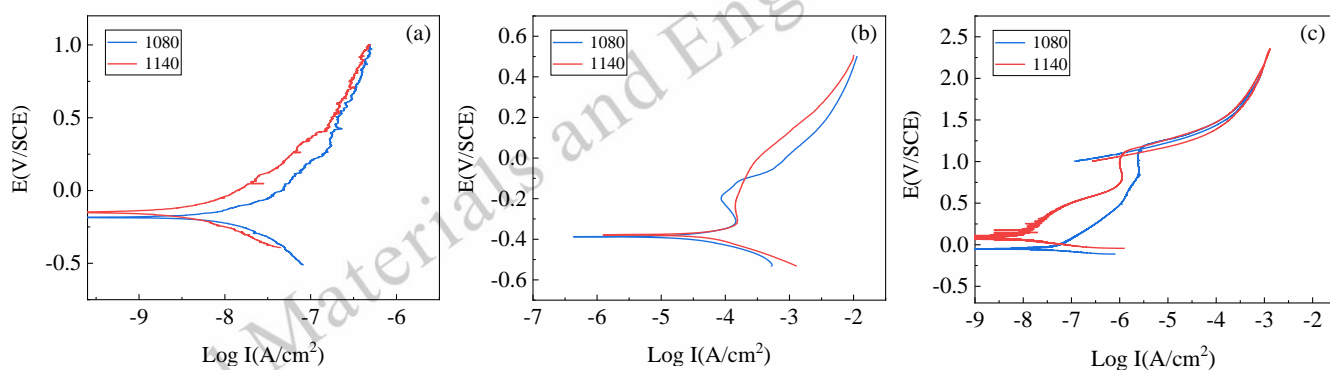
Fig. 7 Potentiodynamic polarization curves of the annealed steels in (a) 100 ppm NaCl solution, (b) 0.36M HCl solution, and (c) H_3BO_3 (B=2700 ppm) solution

The corrosion potential E_{corr}, corrosion current I_{corr} and the calculated corrosion rate V_{corr} were summarized in Table 4. The E_{corr} of the sample 1140 determined by the polarization curve was approximately -0.146 V_{SCE}, which was slightly higher than the value of 1080. Since the Gd-containing phases were more electrochemically active than steel matrix, it was reasonable that the steel containing more M-Gd intermetallics showed higher corrosion current in the anodic region.

Fig. 7(b) shows the potentiodynamic polarization curves of the alloys in a 0.36M HCl solution at 25°C. The anodic current was three or four orders of magnitude larger than the measured values in other solutions. The current was contributed by the severe dissolution of secondary M-Gd phases in HCl solution.

At the potentials larger than -0.3 V_{SCE}, the specimens exhibited passivity and then uniform corrosion of the steel matrix. After the passivity region, the sample 1080 also showed higher corrosion current which indicated that the corrosion rate of the steel in HCl solution was determined by the content of M-Gd phase.

To evaluate the practical corrosion resistance of the duplex stainless steel, it was also tested in a H_3BO_3 (B=2700 ppm) solution. The polarization curves were shown in Fig. 7(c). In this solution, the two specimens exhibited active-passive transition as well. In the region from OCP to passivation voltage, the alloys showed active dissolution. When the applied voltage was increased to 0.8V, passivation occurred. The fitting results shown in Table 4 indicated that the sample 1140 was more corr-

Table 4 Fitting and calculation results based on the potentiodynamic polarization curves

Specimens	E_{corr}/V_{SCE}	$I_{corr}/(A\ cm^{-2})$	$V_{corr}/(g\ m^2\ h^{-1})$
1080 in NaCl solution	-0.182	4.148×10^{-9}	2.887×10^{-5}
1140 in NaCl solution	-0.146	1.023×10^{-9}	0.712×10^{-5}
1080 in HCl solution	-0.386	4.073×10^{-5}	0.281
1140 in HCl solution	-0.376	2.634×10^{-5}	0.183
1080 in H_3BO_3 solution	-0.042	6.501×10^{-8}	4.331×10^{-4}
1140 in H_3BO_3 solution	0.091	2.153×10^{-8}	1.432×10^{-4}

osion-resistant in H_3BO_3 solution. Compared with the results in other two solutions, the difference in E_{corr} and I_{corr} between the samples 1080 and 1140 in H_3BO_3 was the largest.

The corrosion morphologies of the alloys suffered immersion tests in various solutions were characterized by SEM. Fig. 8 is the SEM images of the samples immersed in a NaCl solution for 10 hours. In the two alloys, corrosion was initiated at the Gd-containing phases, while the steel matrix remained intact. According to Figs. 8(b) and (d), it was found that the M_3Gd phase (core part) were more vulnerable to corrosion than the $M_{12}Gd$ phase (shell part). Therefore, we could see that the dissolution of Gd-containing particles was almost at the center area.

Fig. 9 shows the corroded surfaces of the specimens im-

mersed in a 0.36M HCl solution for 4 hours. For the sample 1080 suffered immersion in the acid solution with Cl⁻, it was seen that the M_3Gd core had been preferentially dissolved in some core-shell particles, while some other particles were entirely dissolved. However, for the 1140 specimen, almost all the M-Gd particles were completely corroded. The preferential dissolution of Gd-rich phase is reasonable since the standard electrode potential of Gd (-2.279V versus standard hydrogen electrode[37]) is much lower than others elements in the steel matrix. Gd can form hydroxide ($Gd(OH)_3$) in alkaline solution, but it is difficult to form a stable oxidative protective film in neutral and acidic environments[37]. In our view point, the corrosion rates of the steel samples were mainly determined by the exposed M-Gd intermetallics on steel surface, since they act as weak points dis-

rupting the continuity of passive film. During the corrosion process, dissolution of M-Gd phases leads to the exposure of fresh metal matrix and the following pitting initiation. In HCl solution, we could find that the steel matrix also suffered corrosion attack. Some of the dissolution pits have spread to the steel matrix and trigged pitting corrosion (Fig. 9(b)). According to the observations, the microstructure of the Gd-containing phases may have influence on their corrosion behaviors, and consequently corrosion resistance of the steel. The partial dissolution of the M-Gd phases with core-shell structure is the evidence and underlying mechanism is worthwhile to investigate in the future.

The corroded surface morphology of the two alloys immersed in a H_3BO_3 (B=2700 ppm) solution was examined by SEM as well. Shown in Fig. 10, it is worth noting that most of the M-Gd particles were not dissolved. A close inspection indicated that dissolution preferentially occurred in $M_{12}Gd$ phase (shell part), which was significantly different with the corrosion behaviors of the steels in NaCl and HCl solutions. The observed phenomenon is consistent with Ha et al.'s results[38]. In their work, the Gd-lean phase $((Fe,Ni)_{17}Gd_2)$ showed more severe corrosion morphology after 3 hours immersion in H_3BO_3 solution (B=1748 ppm). They explained that the preferential dissolution of Gd-lean phase in H_3BO_3 solution was due to the affinity between the H_3BO_3 and Gd[39]. In the H_3BO_3 solution with a pH less than 7, the Gd-containing phase could be protected due to the selective adsorption of H_3BO_3 to M-Gd phase and such adsorption is more protective for the Gd-rich phase. This factor may also account for the relatively large difference in the electrochemical corrosion rates between the two alloys in H_3BO_3 solution, as shown in Table 4.
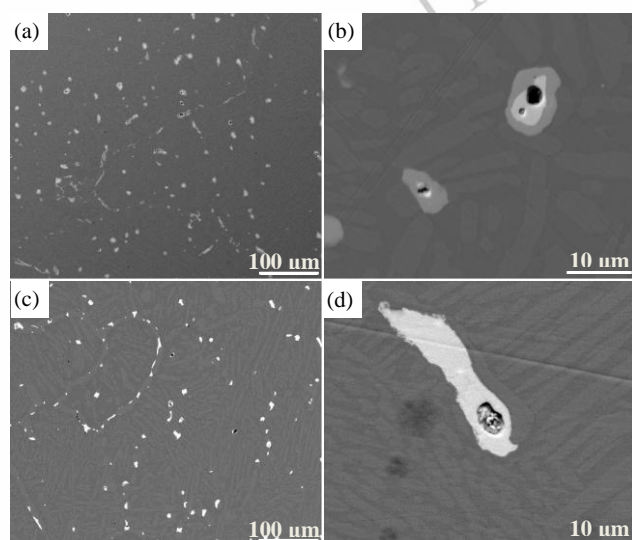

Fig. 8 Corrosion morphologies of the alloys immersed in a 100 ppm NaCl solution at 40°C for 10h: (a) and (b) SEM images of the sample annealed at 1080°C; (c) and (d) SEM images of the sample 1140
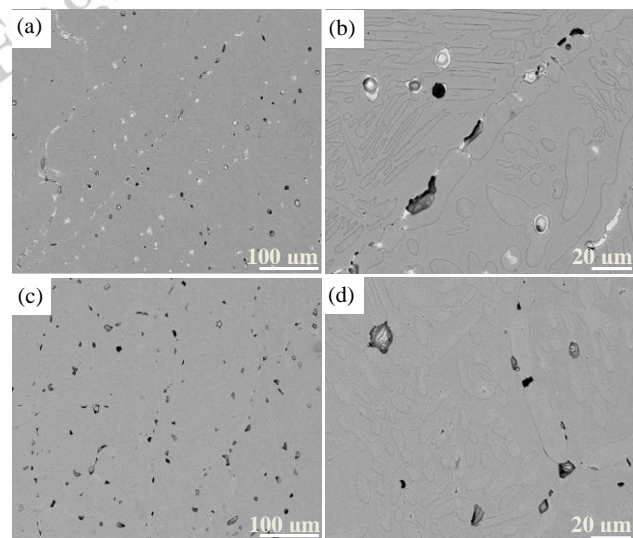

Fig. 9 Corrosion morphologies of the alloys immersed in a 0.36M HCl solution at 40°C for 4h: (a) and (b) SEM images of the sample 1080. It could be seen pitting corrosion of the steel matrix was initiated by the dissolution of M-Gd phase; (c) and (d) SEM images of the sample 1140. Almost all the M-Gd particles were completely dissolved.
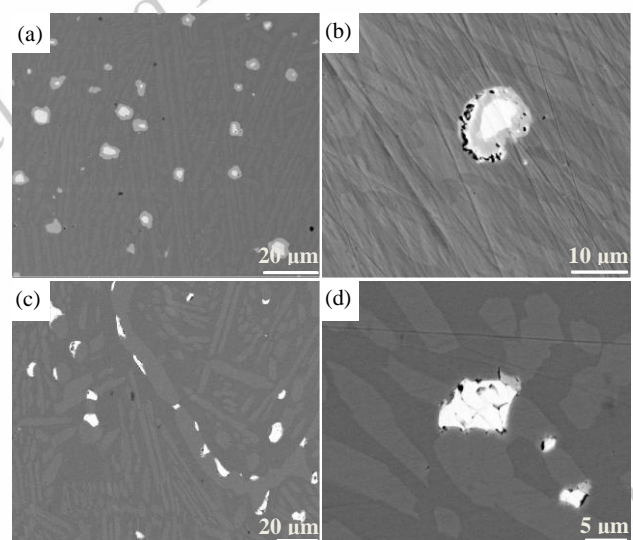

Fig. 10 Corrosion morphologies of the alloys immersed in a (B=2700 ppm) H_3BO_3 solution at 40°C for 3h: (a) and (b) the steel sample annealed at 1080°C; (c) and (d)annealed at 1140°C. In H_3BO_3 solution, the $M_{12}Gd$ phase was preferential dissolved instead of the M_3Gd phase.

3 Conclusions

In this study, the microstructures and corrosion behaviors of the 1.0 wt.%Gd duplex stainless steel with different annealing temperatures were studied. The following conclusions could be drawn:

1) Two types of Gd-containing phases, M_3Gd and $M_{12}Gd$ were identified in the alloys. As the annealing temperature increased, the contents of Gd-containing phases increased firstly

and then decreased. Core-shell structured M-Gd intermetallics and the Gd-rich phase (M_3Gd) were the dominant secondary phases in the sample 1080 and sample 1140, spectively.

2) The corrosion rate of the steels was related to the content of M-Gd intermetallics. The sample 1140 showed better corrosion resistance than the sample 1080.

3) Immersion tests indicated that M_3Gd phase was more electrochemically active compared to $M_{12}Gd$ in NaCl and HCl solutions, but more noble in a H_3BO_3 solutions.

References

1　Soliman S E, Youchison D L, Baratta A J et al. *Nuclear technology*[J], 1991, 96(3): 346

2　Choi Y, Moon B M, Sohn D S. *Nuclear Engineering and Technology*[J], 2013, 45(5): 689

3　Li Aodi, Liang Tian, Zhang Xueliang et al. *Rare Metal Materials and Engineering*[J], 2024, 53(3): 736 (in Chinese)

4　Robino C V, Michael J R, DuPont J N et al. *Journal of materials engineering and performance*[J], 2003, 12: 206

5　Jung M Y, Baik Y, Choi Y et al. *Nuclear Engineering and Technology*[J], 2019, 51(1): 207

6　Kang J Y, Jang J H, Kim S D et al. *Journal of Nuclear Materials*[J], 2020, 542: 152462

7　Stoulil J, Hemmer V, Šefl V et al. *Materials and Corrosion*[J], 2015, 66(4): 342

8　Lister T E, Mizia R E, Pinhero P J et al. *Corrosion*[J], 2005, 61(7): 706

9　Mizia R E, Lister T E, Pinhero P J et al. *Nuclear technology*[J], 2006, 155(2): 133

10　Mizia R E, Lister T E. *Nuclear technology*[J],2011, 176(1): 9

11　DuPont J N, Robino C V, Michael J R et al. *Welding journal*[J], 2004, 83(11): 289

12　Zhou Y T, Zan Y N, Wei X X et al. *Corrosion Science*[J], 2019, 153: 74

13　Zhou Y T, Zan Y N, Wang Q Z et al. *Corrosion Science*[J], 2020, 174: 108808.

14　Zan Y N, Zhang Q, Zhou Y T et al. *Journal of Nuclear Materials*[J], 2019, 526: 151788

15　Chen Hongsheng, Wang Wenxian, Nie Huihui et al. *Rare Metal Materials and Engineering*[J], 2020, 49(12): 4358 (in Chinese)

16　Chen Hongsheng, Wang Wenxian. *Rare Metal Materials and Engineering*[J], 2017, 46(2): 392 (in Chinese)

17　Choi Y, Moon B M, Sohn D S. *Nuclear Engineering and Technology*[J], 2013, 45(5): 689

18　Cetin M, Ölmez E. *Protection of Metals and Physical Chemistry of Surfaces*[J], 2020, 56: 619

19　Gu Mingfei, Huang Dagui, Zhao Yong et al. *Rare Metal Materials and Engineering*[J], 2022, 51(12): 4726 (in Chinese)

20　Ho S L, Yue H, Tegafaw T et al. *ACS omega*[J], 2022, 7(3): 2533

21　Kang Y. R, Lee M W, Kim G N. *Nuclear Science and Engineering*[J], 2015, 180(1): 86

22　Lee S W, Ahn J H, Moon B M et al. *Materials & Design*[J], 2020, 194: 108906.

23　Zhang W, Li C, Su X. *Journal of phase equilibria*[J], 1998, 19(1): 56

24　Saidi M, Walha S, Nouri K et al. *Journal of Alloys and Compounds*[J], 2019, 792: 87

25　Zhang Cheng, Pan Jie, Wang Zixie et al. *Nuclear Engineering and Technology*[J], 2023, 55(5): 1541

26　Qi Z D, Yang Z, Meng X F et al. *Materials Today Communications*[J], 2023, 37: 107315

27　Andersson J O, Helander T, Höglund L et al. *Calphad*[J], 2002, 26(2): 273

28　Wang Yurong, Wu Yu, Li Yongwang et al. *Heat treatment of metals*[J], 2023, 48(02): 200 (in Chinese)

29　Qi Zhengdong, Yang Zhong, Li Jianping et al. *Materials*[J], 2022, 15(9): 3255

30　Khan Z. *Journal of the Southern African Institute of Mining and Metallurgy*[J], 2012, 112(4): 309

31　Ha H Y, Jang J H, Lee T H et al. *Corrosion Science*[J], 2021, 192: 109798

32　Ha H Y, Kim S D, Jang J H et al. *Journal of The Electrochemical Society*[J], 2020, 167(10): 101506

33　Mizia R E, Lister T E, Pinhero P J et al. *Nuclear technology*[J], 2006, 155(2): 133

34　Zhang Shenghan, Lu Quan, Xu Yunfei et al. *International Journal Electrochemical Science*[J],2018, 13:3246

35　Pan Jie, Wang Zixie, Mei Qiliang et al. *Scripta Materialia*[J], 2023, 234: 115575

36　Mizia R E, Lister T E, Pinhero P J et al. *NACE CORROSION*[C], 2003, NACE-03679

37　Murphy G W. *Science*[J], 1966, 154(3756): 1537

38　Ha H Y, Lee T H, Jo H H et al. *Journal of Nuclear Materials*[J], 2023, 578: 154367

39　Horkans J. *Journal of the Electrochemical Society*[J], 1979, 126(11): 1861

含 Gd 不锈钢的时效处理及腐蚀行为

解曼曼 [1,2†]，贾洞箫 [3,4†]，贾茜霖 [2,4]，赵菲 [1]，梁田 [3,5*]，周杨韬 [2*]

(1. 太原科技大学材料科学与工程学院，山西 太原 030024)

(2. 中国科学院金属研究所沈阳材料科学国家研究中心，辽宁 沈阳 110016)

(3. 中国科学院金属研究所师昌绪先进材料创新中心，辽宁 沈阳 110016)

(4. 中国科学技术大学材料科学与工程学院，辽宁 沈阳 110016)

(5. 中国科学院金属研究所核用材料与安全评价重点实验室，辽宁 沈阳 110016)

摘　要：本文研究了含 1 wt.% Gd 不锈钢在不同温度时效后的微观结构与腐蚀行为。研究表明材料中含 Gd 第二相的体积比以 1080℃为转折点，先增后减。在 1080℃时效处理的样品中，主要的第二相为双相 M-Gd 化合物，其核心为 M_3Gd 相，外层为 $M_{12}Gd$ 相。在 1140℃时效处理后，M_3Gd 为其中的主要第二相。同时，我们还研究了这两种样品在 NaCl、HCl 及 H_3BO_3 溶液中的腐蚀行为。1140℃处理后的样品具有相对较低的腐蚀速率。在 NaCl 和 HCl 溶液中，M_3Gd 较 $M_{12}Gd$ 具有较高的电化学活性；而在 H_3BO_3 溶液中，M_3Gd 则较为稳定。

关键词：中子吸收双相不锈钢; 时效处理; 含 Gd 金属间化合物; 腐蚀